Modeling global carbon and water fluxes and hyperspectral canopy radiative transfer simultaneously using a next generation land surface model—CliMA Land

Y. Wang[1], R. K. Braghiere[2,3], M. Longo[2,4], A. J. Norton[2], P. Köhler[1], R. Doughty[1,5], Y. Yin[1], A. A. Bloom[2], and C. Frankenberg[1,2]

[1]Division of Geological and Planetary Sciences, California Institute of Technology, Pasadena, California 91125, USA

[2]Jet Propulsion Laboratory, California Institute of Technology, Pasadena, California 91109, USA

[3]Joint Institute for Regional Earth System Science and Engineering, University of California at Los Angeles, Los Angeles, California 90095, USA

[4]Climate and Ecosystem Sciences Division, Lawrence Berkeley National Laboratory, Berkeley, California 94720, USA

[5]College of Atmospheric & Geographic Sciences, GeoCarb Mission, University of Oklahoma, Norman, Oklahoma 73019, USA

Key Points:

- Hourly carbon and water fluxes, and hyperspectral canopy radiative transfer are simulated simultaneously
- Modeled indices well capture the spatial patterns across the globe
- The model highlights need and possibility of fusing data from multiple sources

Corresponding author: Y. Wang, wyujie@caltech.edu

Corresponding author: A. A. Bloom, alexis.a.bloom@jpl.nasa.gov

Corresponding author: C. Frankenberg, cfranken@caltech.edu

Abstract

Recent progress in satellite observations has provided unprecedented opportunities to monitor vegetation activity on the global scale. However, a major challenge in fully utilizing remotely sensed data to constrain land surface models (LSMs) lies in inconsistencies between simulated and observed quantities. Transpiration and gross primary productivity (GPP) that traditional LSMs simulate are not directly measurable from space and they are inferred from spaceborne observations using assumptions that are inconsistent with those of the LSMs, whereas canopy reflectance and fluorescence spectra that satellites can detect are not modeled by traditional LSMs. To bridge these quantities, we present the land model developed within the Climate Modeling Alliance (CliMA), which simulates global-scale GPP, transpiration, and hyperspectral canopy radiative transfer (RT). Thus, CliMA Land can predict any vegetation index or outgoing radiance, including solar-induced chlorophyll fluorescence (SIF), normalized difference vegetation index (NDVI), enhanced vegetation index (EVI), and near infrared reflectance of vegetation (NIRv) for any given measurement geometry. Even without parameter optimization, the modeled spatial patterns of CliMA Land GPP, SIF, NDVI, EVI, and NIRv correlate significantly with existing observational products. CliMA Land is also very useful in its high temporal resolution, e.g., providing insights into when GPP, SIF, and NIRv diverge. Based on comparisons between models and observations, we propose ways to improve future land modeling regarding data processing and model development.

Plain Language Summary

The land is a big sink of CO_2, but there is not a direct way to measure its carbon sink strength at the global scale. Researchers often use eddy covariance flux tower and/or satellite observations to infer land carbon sink strength. However, the flux towers are too sparsely distributed, and satellites can only detect radiation-related properties of the vegetation such as solar induced chlorophyll fluorescence. We bridge the two aspects by developing a new land surface model that simultaneously simulates both carbon and water fluxes as well as spectrally resolved canopy radiation properties. We compare our model outputs directly to not only carbon flux estimations but also satellite observations. We show that our new land surface model can represent how carbon flux and canopy radiation properties vary across the globe and help understand

how ecosystems work under different environmental conditions. We believe advances in data processing and implementation of new features in land modeling will improve the land surface model predictive skills in the future.

1 Introduction

The land system sequesters approximately 25% of anthropogenic CO_2 emissions (Le Quéré et al., 2018), which slows the increase of atmospheric CO_2 concentration and thus global climate change. However, it is highly uncertain how the strength of terrestrial carbon sink will change in the future given that warmer global temperatures impact vegetation carbon fixation in diverging ways and that higher CO_2 concentration fertilizes leaf photosynthesis (Sperry et al., 2019). Despite the importance of the magnitude of land net CO_2 uptake, overall spatial and temporal global terrestrial carbon sink strength patterns remain poorly understood given the lack of direct observations at the landscape scale globally. As a result, the estimation of the global terrestrial carbon sink is largely dependent on data interpolation and/or modeling.

Gross primary productivity (GPP) is the most direct measure of the gross land carbon sink. However, global scale GPP products from various studies differ dramatically (Anav et al., 2015) due to differences in (i) the model selection, such as stomatal model parameters (Medlyn, Duursma, & Zeppel, 2011), soil moisture response (Powell et al., 2013; Trugman et al., 2018), and canopy structure setup (Braghiere et al., 2019, 2020; Y. Wang & Frankenberg, 2021), and (ii) the major drivers used to force the model, such as flux tower data (e.g., Jung et al., 2011; Tramontana et al., 2016; Jung et al., 2020) or remote sensing data (e.g., Zhang et al., 2017). Furthermore, the rapidly changing climate and increasing atmospheric CO_2 make it more challenging for the models to agree on the magnitude and direction of the future land carbon sink strength (Anav et al., 2013; Arora et al., 2013; Jones et al., 2013; Anav et al., 2015; Zhang & Ye, 2021).

GPP divergence caused by model selection may be considered as a result of the various forms of forcing data. For example, eddy covariance flux towers provide relatively high quality half-hourly carbon and water fluxes (Baldocchi et al., 2001; Baldocchi, 2020), but are too sparsely distributed, and modeler have to rely on data interpolation for global interpretation. Also, GPP is not directly measured but

partitioned from ecosystem net carbon flux using nighttime flux measurements to proxy respiration rates, and this partitioning could result in biased GPP estimates (Wehr et al., 2016). In comparison, spaceborne remote sensing data provide good spatial coverage (Schimel et al., 2015, 2019), but often have coarse temporal resolution and cannot directly measure carbon or water fluxes. Models based on remote sensing often have to rely on empirically correlating GPP with various quantities based on reflectance and/or fluorescence. As a result, a satisfactory approach to parameterize land surface models (LSMs) consistently at the global scale is lacking, and model-observation comparisons are inconsistent. In theory, if the LSMs can correctly account for vegetation processes and are given the same high quality flux and climate forcing data, these models should be able to predict similar GPP once their model parameters (e.g., leaf area index, plant functional type distributions, leaf photosynthetic capacity, and plant hydraulic traits) are optimized for the input training data. Currently, high quality carbon and water flux data are sparse, which makes model parameterization and development challenging and hence their GPP predictions are unreliable. Therefore, a key step for improving land modeling is to integrate data from multiple sources, equip LSMs with corresponding features to simulate observations, and parameterize the LSMs by minimizing the model-data mismatch.

Remotely sensed data that are useful to constrain land processes at regional and global scales are mostly based on observed reflected and emitted radiances and optical depths of vegetation canopies (e.g., Badgley et al., 2017; Sun et al., 2017; Konings et al., 2021). Among the various index and radiance measures, solar-induced chlorophyll fluorescence (SIF) and near infrared reflectance of vegetation (NIRv) are the two most promising candidates for estimating GPP given their overall good correlations with GPP (Frankenberg et al., 2011; Badgley et al., 2017; Sun et al., 2018; Badgley et al., 2019; Doughty et al., 2021). Nevertheless, the intermediate step of translating SIF and/or NIRv to GPP may introduce additional biases given the decoupled correlations among them in light saturated environments (Zhang et al., 2016), drought stressed conditions (Helm et al., 2020), cold winters (Magney et al., 2019), and over diversely structured vegetation (Braghiere et al., 2021).

Alternatively, a better way to utilize the remote sensing data would be to match modeled canopy fluorescence and reflectance spectra to satellite retrievals directly (Norton et al., 2018; Shiklomanov et al., 2021; Y. Wang, Köhler, et al., 2021). This,

however, requires LSMs to move from simple broadband canopy radiative transfer (RT) to a hyperspectral canopy RT in order to utilize spectrally resolved remote sensing data (e.g., Norton et al., 2019), which most existing LSMs are not designed to do. We note that traditional LSMs can be extended to utilize satellite data through scaling leaf level SIF up to canopy level using two leaf radiation scheme (e.g., Qiu et al., 2019). However, this empirical approach discards useful information that the hyperspectral and multi-layer approach contains, such as the sun-sensor geometry and vertical canopy gradients in fluorescence and photosynthesis yields, which interact non-linearly.

Our recent efforts bridge land modeling and observations together in a new LSM as part of a new generation earth system model within the Climate Modeling Alliance, CliMA (`https://clima.caltech.edu`; Y. Wang, Köhler, et al., 2021). The new model can simulate hyperspectral canopy RT in a multi-layer canopy, enabling us to simultaneously simulate canopy carbon and water fluxes as well as corresponding canopy fluorescence and reflectance spectra. Our new LSM, CliMA Land, improves the representation of SIF at the canopy scale (Braghiere et al., 2021) and well captures the carbon and water fluxes measured at flux tower sites (Y. Wang, Köhler, et al., 2021). In particular, the simultaneously simulated GPP, SIF, and NIRv allow for many potential studies that are not possible in the past, say the diurnal cycles and correlations among SIF, NIRv, and GPP at various temporal resolutions.

In this study, we (i) describe the general model framework of CliMA Land, (ii) detail the model parameterization and simulation procedure, and (iii) show our first global run using CliMA Land, the first LSM that outputs hourly canopy fluorescence and reflectance spectra along with corresponding carbon and water fluxes. In section 3, we investigate how well CliMA Land GPP, SIF, and other reflectance indices capture their spatial patterns. We run our model for the years 2010 and 2019, and compare our model outputs with flux tower observation-based datasets for the year 2010 and with other satellite-based GPP and SIF products for the year 2019. Finally, we discuss potential ways to improve future land modeling using the new LSM framework.

2 Materials and Methods

To facilitate research with various scales and model selections, CliMA Land is highly modular, containing plant hydraulics, stomatal control, canopy RT, and

soil-plant-air continuum sub-modules, each of which can be used as a standalone package (Figure 1; Y. Wang, Köhler, et al., 2021; Y. Wang & Frankenberg, 2021). Through simulating hyperspectral canopy RT and scaling leaf level gas exchange, we can integrate total canopy carbon and water fluxes, and simulate a number of remotely sensible quantities (such as SIF and NIRv) simultaneously at arbitrarily fine time steps at the global scale (here for the Nadir viewing satellite direction). CliMA Land code and documentation are publicly and freely available at `https://github.com/CliMA/Land` (the exact version of model is archived at Y. Wang, Braghiere, & Frankenberh, 2021, last access: 15 Nov 2021). Below, we describe the general CliMA Land framework and the procedure we used for the global simulations.

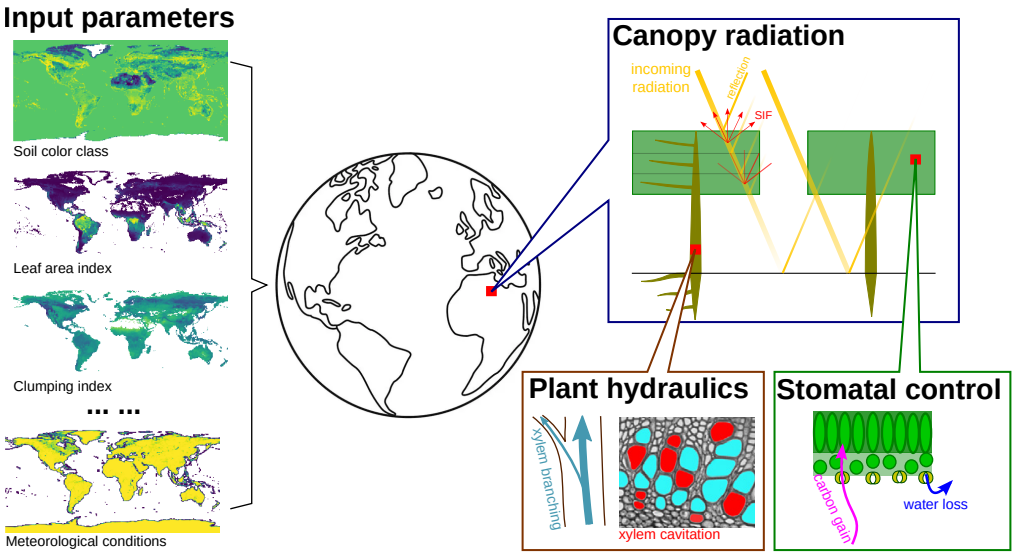

Figure 1. Diagram of the model framework and parameterization of CliMA Land. CliMA Land consists of three key modules: canopy radiative transfer (RT), plant hydraulics, and stomatal control. Canopy RT module is responsible for canopy RT simulation; plant hydraulic module accounts for the water movement from soil to the air; stomatal control module addresses the leaf gas exchange. To run CliMA Land at the global scale, various input parameters are used to initialize the site such as soil color class, leaf area index, clumping index, and meteorological conditions. Then each site is treated as a bulk forest with bulk plant traits, and carbon and water fluxes and canopy spectra are simulated using the soil-plant-air continuum model.

2.1 CliMA Land

CliMA Land (v0.1; Y. Wang, Köhler, et al., 2021) considers a grid cell (e.g., a $1^\circ \times 1^\circ$ grid) as a "mono-species" stand in which all plants have the same size with a suite of bulk properties (such as canopy height, clumping index, and leaf chlorophyll content; Figure 1). CliMA Land supports freely customized plant hydraulic system ranging from a single organ (e.g., leaf, stem, or root) to a whole plant (such as grass and tree). CliMA Land also features a variety of stomatal models from empirical approaches (e.g., Ball et al., 1987; Medlyn, Duursma, Eamus, et al., 2011) to stomatal optimization theories (e.g., Sperry et al., 2017; Y. Wang et al., 2020). Further, CliMA Land can simulate canopy RT using either the traditional two leaf RT approach by partitioning the canopy to sunlit and shaded fractions with broadband radiative transfer scheme (Campbell & Norman, 1998), or a more complex multi-layer canopy model that accounts for hyperspectral radiation, leaf angular distribution and canopy clumping (Yang et al., 2017; Braghiere et al., 2021; Y. Wang, Köhler, et al., 2021; Yang et al., 2021).

2.1.1 Plant Hydraulic Architecture

Plant hydraulics in CliMA Land is simulated numerically by partitioning the plant into root, stem, and leaf organs (Sperry & Love, 2015; Sperry et al., 2016), and a specific xylem vulnerability curve is used for each organ (the curve is allowed to differ within and among organs). The organs can be aligned in a flexible way (Y. Wang, Köhler, et al., 2021). For example, a tree comprises a multi-layer root system, a trunk (stem), a multi-layer canopy system (stem and leaf in series in each layer); a grass comprises a multi-layer root system and a multi-layer canopy system (only leaf is present in each layer). Further, the plant hydraulics sub-module allows for customizing root and stem height change, and thus is able to account for a gravitational pressure drop in the xylem (Y. Wang, Köhler, et al., 2021). Moreover, there is a drought legacy variable in each hydraulic organ (the xylem remembers the minimal xylem pressure and thus minimal hydraulic conductance it has experienced, and xylem hydraulic conductance is not allowed to be higher than this memory conductance due to irreversible xylem cavitation), and addressing this gives more realistic stomatal response to the environment after a drought (W. R. L. Anderegg et al., 2015; Y. Wang et al., 2020). We also account for temperature effects on water viscosity and surface

tension in our model, which could otherwise result in non-negligible simulated water transport biases (e.g., 1 °C difference in water temperature potentially results in c. 2.4% change in maximum hydraulic conductance; Reid et al., 1987).

Plant hydraulic architecture may impact the stomatal models in CliMA Land (not always as some stomatal models do not rely on plant hydraulics at all, see examples in section 2.1.2). With the ascent of sap along the xylem, xylem water pressure typically gets more and more negative, potentially resulting in xylem cavitation. The higher the water flux in the xylem and/or the drier the soil, the higher the risk of xylem cavitation. Loss of plant water transport capability may harm plants' leaf gas exchange performance given the limited water supply to leaves, and thus plants may regulate their stomata to alleviate the risk (Sperry & Love, 2015). Combining photosynthetic carbon gain and hydraulic risk leads to a variety of stomatal optimization models that simulate stomatal behavior using plant traits rather than empirically fitted parameters (see Y. Wang et al. (2020) for an overview). Furthermore, plant hydraulic status is also used in more and more empirical stomatal models (e.g., Kennedy et al., 2019), acting as a tuning factor to link stomatal responses to soil moisture status.

2.1.2 Stomatal Control

Stomatal behavior in CliMA Land can be simulated using either empirical models that rely on statistically fitted parameters or stomatal optimization models that are based on plant traits and processes. To date, CliMA Land embeds three published empirical stomatal models, namely the Ball et al. (1987), Leuning (1995), and Medlyn, Duursma, Eamus, et al. (2011) models. These empirical models can be used along with two general types of tuning factors to force stomatal response to drought, one of which takes effect through tuning the empirical model parameters (such as the slope parameter g_1) and another takes effect via down-regulating photosynthetic capacity (e.g., Kennedy et al., 2019). CliMA Land also supports four published stomatal optimization models based on plant hydraulics given their best performance in three datasets (W. R. Anderegg et al., 2018; Venturas et al., 2018; Y. Wang et al., 2019), and they are Sperry et al. (2017), W. R. Anderegg et al. (2018), Eller et al. (2018), and Y. Wang et al. (2020) models. These optimization based models are less dependent on fitting parameters and performed well compared to empirical models, though are more

difficult to parameterize. Further, the optimization framework can be extended to account for nighttime transpiration responses to the environment (Y. Wang, Anderegg, et al., 2021), showing great potential in advancing land surface modeling.

Despite the predictive skills of optimization models in predicting stomatal responses to the environment, particularly soil moisture, difficulties in parameterizing these models hamper the use of trait- and optimization-based stomatal models at global scales. As a result, empirical models are still the top candidates for land surface models before reliable spatially resolved hydraulic trait maps become available. Similarly, tuning empirical model parameter g_1 or photosynthetic capacity based on plant hydraulics does not work either. For example, D. M. Lawrence et al. (2019) and Kennedy et al. (2019) proposed to use hydraulic conductance to tune leaf photosynthetic capacity; however, the calculation of hydraulic conductance relies on the xylem vulnerability curve as well as whole plant hydraulic conductance, which are spatially unknown at global scales at present. Thus, to date, simulating global land carbon and water fluxes is still limited to empirical models and tuning factors based on soil conditions rather than plant hydraulics. However, with CliMA Land, we provide more alternatives that can be used in the future when globally spatial hydraulic trait maps become available or can be inferred using, for instance, evapotranspiration measurements or skin temperature in general.

2.1.3 Canopy Radiative Transfer

CliMA Land features two possible canopy RT schemes: single layered two leaf RT model with sunlit and shaded fractions simulating broadband reflectance and transmittance (Campbell & Norman, 1998), and a vertically layered canopy model with leaf angular distribution simulating hyperspectral reflectance and transmittance (adapted from Soil Canopy Observation of Photosynthesis and Energy fluxes model, SCOPE van der Tol et al., 2009; Yang et al., 2017). While the inclusion of the two leaf canopy RT model allows for compatibility with other vegetation models, the use of a complex multi-layer canopy model enables the simulation of canopy reflectance and fluorescence as well as carbon and water fluxes simultaneously, promoting the integration of land models with remote sensing observations (Y. Wang, Köhler, et al., 2021). Moreover, the multi-layer canopy model also supports vertically resolved heterogeneous micro-climates and leaf physiology within the canopy (Bonan et al.,

2018, 2021; Y. Wang & Frankenberg, 2021). Future research aiming to quantitatively understand the vertical canopy layout (such as optimal nutrient and leaf area partitioning) will further improve the predictive skills of the land surface models.

Compared to the original SCOPE canopy RT scheme, (1) we implemented a clumping index in CliMA Land to account for the horizontal heterogeneity in the canopy (Pinty et al., 2006; Braghiere et al., 2019, 2020). The inclusion of a clumping index can promote light scattering into lower canopy layers, and improves model predictive skills against benchmark 3D datasets (Braghiere et al., 2021). (2) We accounted for carotenoid absorption as absorbed photosynthetically active radiation by the antenna systems, thus photosynthesis and chlorophyll fluorescence (Y. Wang, Köhler, et al., 2021). (3) We converted energy flux to photon flux and computed SIF in terms of photon (to use with fluorescence quantum yield); and then we convert SIF photon flux back to energy flux in the SIF radiative transfer (Y. Wang & Frankenberg, 2021). (4) In the present study, we further expand the soil albedo implementation to hyperspectral simulations to make land modeling more realistic in terms of canopy RT and gas exchange simulations. In brief, soil albedo values at photosynthetically active radiation (PAR) region and near infrared (NIR) regions, denoted as α_{PAR} and α_{NIR} respectively, are calculated by linearly interpolating the reference values at completely wet and dry soils (see Note S1 for more details):

$$\alpha_{\text{PAR}} = \alpha_{\text{PAR,wet}} \cdot \text{RSWC} + \alpha_{\text{PAR,dry}} \cdot (1 - \text{RSWC}), \tag{1}$$

$$\alpha_{\text{NIR}} = \alpha_{\text{NIR,wet}} \cdot \text{RSWC} + \alpha_{\text{NIR,dry}} \cdot (1 - \text{RSWC}), \tag{2}$$

where RSWC is the relative volumetric soil water content (0 when completely dry, 1 when soil water content is saturated), the subscript "wet" denotes saturated soil, and the subscript "dry" denotes completely dry soil.

2.2 Model Parameterization

2.2.1 Soil and Air

Soil color impacts soil albedo calculations and thus canopy RT and gas exchange. We used the Community Land Model soil color class map (data from P. J. Lawrence & Chase, 2007) and soil albedo reference table (Table 3.3 in CLM5 tech notes) to describe broadband soil albedo values at PAR and NIR regions. Note here that CliMA Land supports using either broadband or hyperspectral soil albedo. When hyperspectral soil

albedo scheme was selected, we extrapolated the broadband α_{PAR} and α_{NIR} to a hyperspectral spectrum by fitting the mean hyperspectral α_{PAR} to broadband α_{PAR} and hyperspectral α_{NIR} to a flat constant α_{NIR} in the NIR region using the characteristic curves from (Jiang & Fang, 2019) (see Note S1 for more details):

$$\min \left[\left(\overline{\alpha_{\mathrm{PAR,mod}}} - \alpha_{\mathrm{PAR,ref}} \right)^2 + \left(\overline{\left| \alpha_{\mathrm{NIR,mod}} - \alpha_{\mathrm{NIR,ref}} \right|} \right)^2 \right] \tag{3}$$

The same soil color class map was used for simulations at different years of global run.

Soil hydraulic parameters impact soil water stress to plants (and thus stomatal and SIF responses to soil moisture). We used the van Genuchten equation to describe soil hydraulic parameters (van Genuchten, 1980). We used gridded van Genuchten parameters including soil retention curve characteristic parameters (soil air entry suction and soil pore-size distribution), residual soil water content, and saturated soil water content (data from Dai et al., 2019). The soil hydraulic dataset includes van Genuchten parameters for 4 soil layers, with the layer boundaries range from a soil depth from 0 to 0.1, 0.35, 1, and 3 m; and we partitioned plant root layering accordingly to 4 layers. The same soil van Genuchten parameter map was used for simulations at different years. Eventually, we will be able to use arbitrary vertical resolutions and solve the Richard's equation in both 1D and 3D.

Atmospheric CO_2 concentration impacts leaf level gas exchange and SIF simulation. We used the annual mean CO_2 concentration for each year regardless of the spatial and temporal variations within a year (data from `https://gml.noaa.gov/ccgg/trends/data.html`). A global mean CO_2 concentration was used for simulations at the specific year (e.g., 389 ppm in 2010, and 410 ppm in year 2019).

Climate forcing impacts the plants' stomatal opening and photosynthesis kinetics, and thus carbon and water fluxes as well as canopy reflectance and fluorescence spectra. We downloaded hourly reanalysis weather data with $0.25^\circ \times 0.25^\circ$ spatial resolution from the ERA5 data portal (Hersbach et al., 2018, 2020), and used it to force CliMA Land simulation, i.e. canopy temperature and humidity are currently prescribed but will be dynamically coupled to the atmosphere in the future. The ERA5 reanalysis data we used included wind speed at 10 m (used to determine leaf boundary layer thickness), dew point temperature and air temperature at 2 m (used to compute atmospheric vapor pressure deficit), skin temperature (prescribed, used as a

proxy for leaf temperature), mean direct and total surface shortwave radiation (used to compute direct and diffuse radiation to feed to canopy RT), surface atmosphere pressure, and soil temperature and volumetric water content at four soil layers. Note that the soil layering of ERA5 differs slightly from the soil hydraulic parameters in that the layer boundaries of the ERA5 data range from 0 to 0.07, 0.28, 1, and 2.89 m, and we used the van Genuchten parameters from the soil map in Dai et al. (2019) despite the minor mismatch in soil depth profiles.

2.2.2 Plant Traits

As the pigments that absorb PAR in the antenna system, chlorophyll and carotenoid contents impact leaf-level reflectance and transmittance, and canopy-level radiative transfer and thus leaf gas exchange. We used weekly mean leaf chlorophyll contents to represent seasonality of canopy greenness (data from Croft et al., 2020), and assumed leaf carotenoid content being 1/7 of the chlorophyll content (Croft et al., 2020). We note that the ratio between carotenoid and chlorophyll can be highly variable, and future research into their spatial and temporal variability will make the simulations more accurate. The weekly mean chlorophyll content was averaged from values in the same week from multiple years, and thus the same leaf chlorophyll content dataset was used for simulations at different years.

Leaf mass per area (LMA) impacts reflectance and transmittance of a leaf, and canopy RT and hence leaf gas exchange. We used a globally gridded specific leaf area (SLA = 1/LMA) in our global land model run (Butler et al., 2017). The same LMA dataset was used for simulations at different years of global run.

Leaf photosynthetic capacity impacts leaf gas exchange and fluorescence quantum yield. We used the leaf photosynthetic capacity (represented by maximum carboxylation rate at a reference temperature of 25 °C—V_{cmax25}) from a recent machine learning based product (Luo et al., 2021). The V_{cmax25} was assumed time-invariant. Maximum electron transport rate at a reference temperature of 25 °C—J_{max25} and respiration rate at a reference temperature of 25 °C—R_{d25} were scaled from V_{cmax25} in that $J_{\mathrm{max25}} = 1.67 \cdot V_{\mathrm{cmax25}}$ and $R_{\mathrm{d25}} = 0.015 \cdot V_{\mathrm{cmax25}}$, consistently with (Sperry et al., 2017). We assumed constant $J_{\mathrm{max25}} : V_{\mathrm{cmax25}}$ and $R_{\mathrm{d25}} : V_{\mathrm{cmax25}}$ ratios due to the lack of global datasets, however we note that there is evidence that they vary across the globe

(e.g., Walker et al., 2014; Norby et al., 2017). The same photosynthetic capacity dataset was used for simulations at different years.

Leaf area index (LAI) impacts canopy RT and whole plant gas exchange. We used the gridded Moderate Resolution Imaging Spectroradiometer (MODIS) LAI product at $0.5^\circ \times 0.5^\circ$ spatial resolution and 8-day temporal resolution (data from Yuan et al., 2020). See Yuan et al. (2011) for more details of the LAI data quality control and gap filling. A time-dependent LAI was used in the simulations at the specific year years (e.g., LAI time series at year 2010 was used for the global simulation at year 2010).

Canopy height impacts plant hydraulic architecture and thus leaf gas exchange. We used a globally resolved canopy height map to initialize plant hydraulic architecture within each simulated grid (Simard et al., 2011). If average plant height within the simulated grid was higher than 2 m, we treated the bulk plant as a tree (gravitational pressure drop was accounted for in the stem xylem); otherwise, we treated the bulk plant as a grass (gravitational pressure drop was ignored in the stem xylem). The same canopy height dataset was used for simulations at different years.

The clumping index impacts canopy RT and thus leaf gas exchange. We used a globally gridded clumping index to describe the horizontal canopy heterogeneity for each simulated grid (a constant clumping index for each pixel that does not change within and among growing seasons; He et al., 2012). The same canopy clumping index dataset was used for simulations in different years.

2.2.3 Land Masks

Stand elevation impacts atmospheric pressure, and thus leaf gas exchange. We used the elevation map from (Yamazaki et al., 2017) to initialize the land model at different grids.

Percentage of land in a grid impacts the scaled fluxes in a grid. We used the land-sea mask at $0.25^\circ \times 0.25^\circ$ resolution from ERA5 reanalysis data (Hersbach et al., 2018).

The plant functional type (PFT) distribution impacts bulk properties of a site (such as the empirical slope parameter g_1), and thus stomatal responses to the

environment. We used the CLM PFT distribution map (P. J. Lawrence & Chase, 2007) to derive the empirical parameter g_1 at each grid cell. For each grid, we calculated the weighted g_1 based on the PFT distribution (g_1 for each PFT from De Kauwe et al., 2015). The same PFT distribution map was used for simulations at different years in the present study.

2.3 Global Simulations

We ran CliMA Land globally at $1^\circ \times 1^\circ$ spatial resolution and an hourly temporal resolution. We partitioned the Earth into 360 (in longitude) $\times$ 180 (in latitude) grids, and regridded the model parameters spatially by averaging all the data that fell into the target grid. For each pixel, we read data from the regridded model inputs as in section 2.2, and performed the annual simulation if (1) none of the input data was missing and (2) the pixel was vegetated. A total of 11288 grids were identified after applying these filtering criteria.

For each grid, at each time step, we computed soil water potential for each soil layer (Ψ_i), and the tuning factor using $\frac{\Psi_\mathrm{max} - \Psi_\mathrm{i}}{\Psi_\mathrm{max} - \Psi_\mathrm{min}}$ for each soil layer ($\Psi_\mathrm{max} = 0$ MPa, and $\Psi_\mathrm{min} = -5$ MPa by default). Then, we averaged the tuning factor for all soil layers, and used it along with the g_1 parameter of the Medlyn, Duursma, Eamus, et al. (2011) model to simulate stomatal conductance. We did not use stomatal optimization models in the present study because of the lack of global plant hydraulic trait maps. We ran CliMA Land at steady state, and saved the model predicted hourly GPP, transpiration, SIF at 683/740/757/771 nm (SIF_{683}, SIF_{740}, SIF_{757}, and SIF_{771}, respectively), normalized difference vegetation index (NDVI), enhanced vegetation index (EVI), and NIRv (Badgley et al., 2017):

$$\mathrm{NDVI} = \frac{\alpha_\mathrm{NIR} - \alpha_\mathrm{RED}}{\alpha_\mathrm{NIR} + \alpha_\mathrm{RED}}, \tag{4}$$

$$\mathrm{EVI} = 2.5 \cdot \frac{\alpha_\mathrm{NIR} - \alpha_\mathrm{RED}}{\alpha_\mathrm{NIR} + 6 \cdot \alpha_\mathrm{RED} - 7.5 \cdot \alpha_\mathrm{BLUE} + 1}, \tag{5}$$

$$\mathrm{NIRv} = \mathrm{NDVI} \cdot \alpha_\mathrm{NIR}, \tag{6}$$

where α is the albedo at the given wavelength (BLUE: 469 nm, RED: 645 nm, and NIR: 858.5 nm). We ran the simulations for the years 2010 and 2019.

2.4 Benchmarks

2.4.1 GPP

We compared CliMA Land predicted global GPP for year 2019 against the GPP product interpolated from flux tower using machine learning (MPI GPP; data from Tramontana et al., 2016). We selected and regridded the $0.5^\circ \times 0.5^\circ$ MPI GPP at year 2019 that was based on (1) ensembles that include GPP and terrestrial ecosystem respiration from all flux partitioning methods, (2) ensembles that include carbon fluxes from all machine learning methods, and (3) all carbon fluxes from remote sensing, RS (RS GPP does not use meteorological forcing data). The data was labeled as "GPP.RS_V006.FP-ALL.MLM-ALL.METEO-NONE" as noted at `https://www.fluxcom.org/CF-Download/`. It is worth noting that the MPI GPP is a machine-learning based upscaling of flux tower derived GPP (not true measurements), and that we compared CliMA GPP to this reference dataset rather than to flux tower derived GPP directly.

2.4.2 SIF

We compared CliMA Land predicted mean SIF_{683} and SIF_{740} to the daily average SIF_{683} and SIF_{740} retrieved using the TROPOspheric Monitoring Instrument, TROPOMI (data from Köhler et al., 2018; Doughty et al., 2021). We compare CliMA mean SIF_{757} and SIF_{771} to the daily average SIF_{757} and SIF_{771} retrieved using the Orbiting Carbon Observatory 2, OCO-2 (Sun et al., 2017). Note here that TROPOMI and OCO-2 SIF was averaged from observations with different sun-sensor geometry and that the day length correction was made with the assumption that SIF is function of the cosine of the solar zenith angle. In comparison, CliMA SIF was modeled at nadir direction (viewing zenith angle is 0°), and the day length correction was made by averaging all modeled SIF at different times of a day.

2.4.3 NDVI, EVI, and NIRv

We compared CliMA Land predicted NDVI, EVI, and NIRv to those retrieved using the Moderate Resolution Imaging Spectroradiometer (MODIS) satellites MCD43A4 v006 dataset (Schaaf & Wang, 2015; Doughty et al., 2021). Note that MODIS MCD43A4 v006 reflectance indices have been corrected to nadir direction, which agrees

with CliMA Land simulations. We regridded the MODIS MCD43A4 v006 to global scale NDVI, EVI, and NIRv with 1 degree spatial resolution and 8 day temporal resolution.

2.4.4 ILAMB

We used the International Land Model Benchmarking (ILAMB, v2.6) package for model assessment (Collier et al., 2018) focusing on global patterns of GPP (generated by Artificial Neural Networks and forced with CRUNCEPv6 meteorological data and MODIS; this reference GPP data was different from the one mentioned above, and the GPP is labeled as "GPP.ANN.CRUNCEPv6" Tramontana et al., 2016; Jung et al., 2017) and FLUXNET2015 (Pastorello et al., 2020). To distinguish this product from the one used above, we labeled it as MPI RS+METEO GPP. We also compared CliMA GPP to that from eight Coupled Model Intercomparison Project (CMIP) version 5 models and twelve CMIP version 6 models (Table S1).

We benchmarked the ILAMB overall score for the absolute values, as well as the individual components: the spatially integrated bias score, the root-mean-squared error (RMSE) score (doubly weighted in the overall score to emphasize its importance), the phase shift score, the inter-annual variability score, and the spatial distribution score. For the complete set of equations of each score and further details refer to Collier et al. (2018).

3 Results

3.1 Seasonal cycles

CliMA Land simulated the characteristic seasonal cycles of carbon and water fluxes, and canopy reflectance and fluorescence (Figure 2). In general, the simulated SIF and NIRv tracked the simulated variations of GPP well for the eight selected grids with flux towers located within, except for some drought spells (e.g., days 150–350 in Figure 2b; Marengo et al., 2021), as SIF and NIRv are less sensitive to the environmental stress than GPP (Magney et al., 2020; Marrs et al., 2020). We refer the readers to (Y. Wang, Braghiere, & Frankenberh, 2021) for videos of the hourly CliMA GPP, SIF, and NIRv for the year 2019.

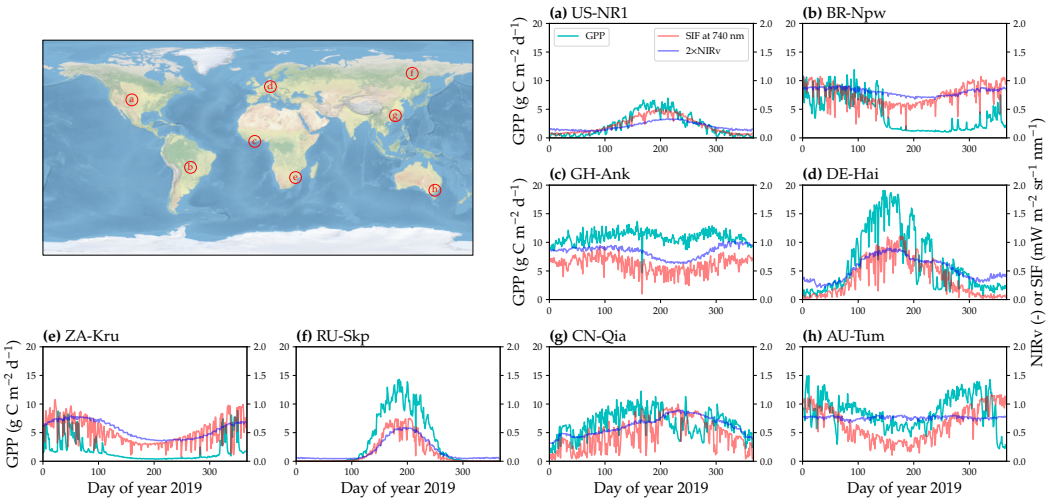

Figure 2. Example of CliMA Land run at eight sites across the globe. CliMA Land global run was made for year 2019. The [latitude, longitude] centers are **(a)** [40.5, −105.5], **(b)** [−16.5, −56.5], **(c)** [5.5, −2.5], **(d)** [51.5, 10.5], **(e)** [−25.5, 31.5], **(f)** [62.5, 129.5], **(g)** [26.5, 115.5], and **(h)** [−35.5, 148.5], respectively. There is a flux tower within each example grid, and they are US-NR1, BR-Npw, GH-Ank, DE-Hai, ZA-Kru, RU-Skp, CN-Qia, and AU-Tum, respectively. The cyan curve plots the modeled daily cumulative gross primary productivity (GPP); the red curve plots the modeled daily mean solar-induced chlorophyll fluorescence (SIF) at 740 nm; the blue curve plots the modeled daytime mean near infrared reflectance of vegetation (NIRv). NIRv is scaled to 2 times the original value to facilitate visualization. GPP, SIF, and NIRv are all daily means (nighttime values set to 0 for GPP and SIF).

3.2 GPP

CliMA GPP displayed reasonable spatial patterns across the globe: reproducing the patterns of MPI GPP which was interpolated from flux tower estimates (Figure 3). CliMA GPP and MPI GPP differed in their magnitudes (Figure 3), and CliMA annual mean GPP, on average, was higher than that of MPI GPP by about 63% ($y = 1.629x + 0.024$ and $R^2 = 0.806$ for the linear regression in Figure 3; slope significantly different from 1, $p < 0.001$). The CliMA Land predicted a global GPP of 160.0 Pg C year^{-1}, whereas the reference MPI GPP was 126.8 Pg C year^{-1}.

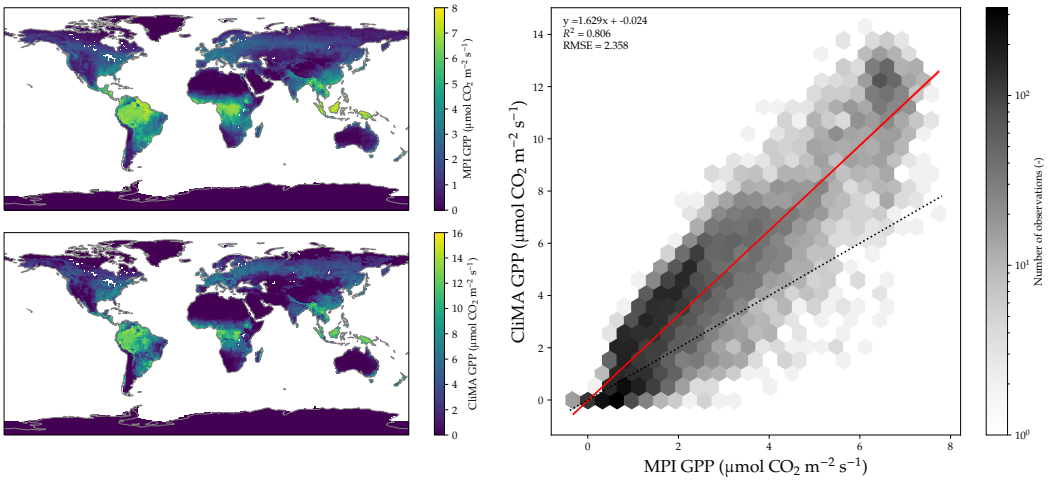

Figure 3. Comparison of gross primary productivity (GPP). CliMA Land global run was made for the year 2019. MPI GPP was interpolated from flux tower estimates using machine learning. GPP was annual means averaged from monthly averages (nighttime values set to 0). Red solid line with shaded region plots the linear regression with confidence intervals, and black dotted line plots the 1:1 line.

3.3 SIF

CliMA SIF_{683} agreed well with observed spatial patterns of TROPOMI SIF_{683}, though the two differed in their magnitude (Figure 4). CliMA SIF_{683} was generally higher than TROPOMI SIF_{683} given the negative TROPOMI SIF_{683} values (Figure 4). The regression slope was close to 1 ($y = 1.074x + 0.054$ and $R^2 = 0.492$; slope significantly different from 1, $p < 0.001$).

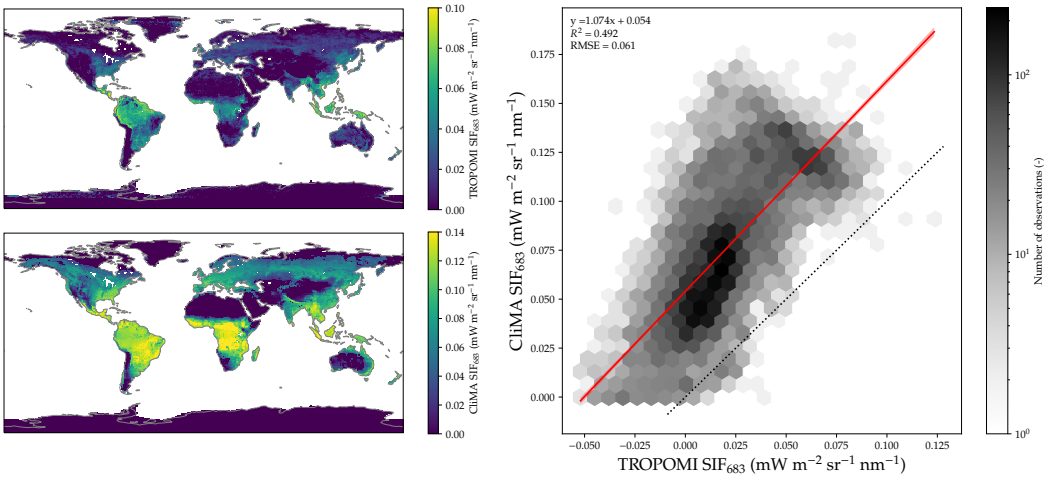

Figure 4. Comparison of solar induced chlorophyll fluorescence at 683 nm (SIF_{683}). CliMA Land global run was made for the year 2019. TROPOMI SIF_{683} was regridded from satellite retrievals. SIF_{683} was annual means averaged from monthly averages (nighttime values set to 0). Red solid line with shaded region plots the linear regression with confidence intervals, and black dotted line plots the 1:1 line.

Similarly, CliMA SIF_{740} also well matched the spatial patterns of TROPOMI SIF_{740}, though the two also differed in their magnitudes (Figure 5). Slope of the regression between the two was close to 1 ($y = 1.263x + 0.118$ and $R^2 = 0.495$; slope significantly different from 1, $p < 0.001$).

When compared to OCO-2 SIF_{757}, while CliMA SIF_{757} well represented the spatial patterns, it predicted dramatically higher SIF_{757} than OCO-2 retrievals ($y = 1.946x + 0.044$ and $R^2 = 0.681$; slope significantly different from 1, $p < 0.001$; Figure 6). The dramatically different magnitudes suggested potential issue in CliMA Land SIF model or OCO-2 SIF_{757} retrieval algorithm.

For SIF at 771 nm, CliMA SIF_{771} also well tracked the spatial patterns of OCO-2 SIF_{771}, and the magnitude differed less than that for SIF_{757} ($y = 1.392 + 0.039$ and $R^2 = 0.633$; Figure 7). Though the slope was close to 1, it was still significantly different from 1 ($P < 0.001$).

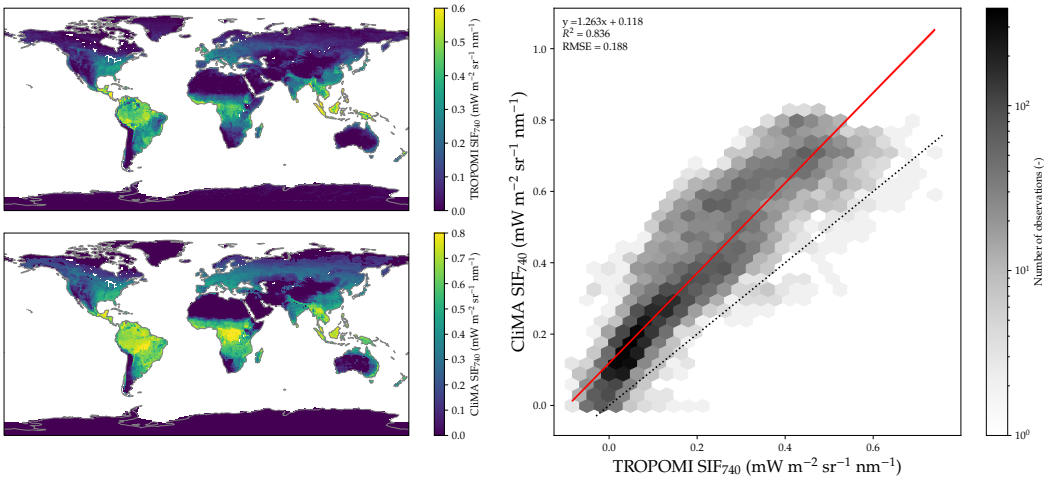

Figure 5. Comparison of solar induced chlorophyll fluorescence at 740 nm (SIF_{740}). CliMA Land global run was made for the year 2019. TROPOMI SIF_{740} was regridded from satellite retrievals. SIF_{740} was annual means averaged from monthly averages (nighttime values set to 0). Red solid line with shaded region plots the linear regression with confidence intervals, and black dotted line plots the 1:1 line.

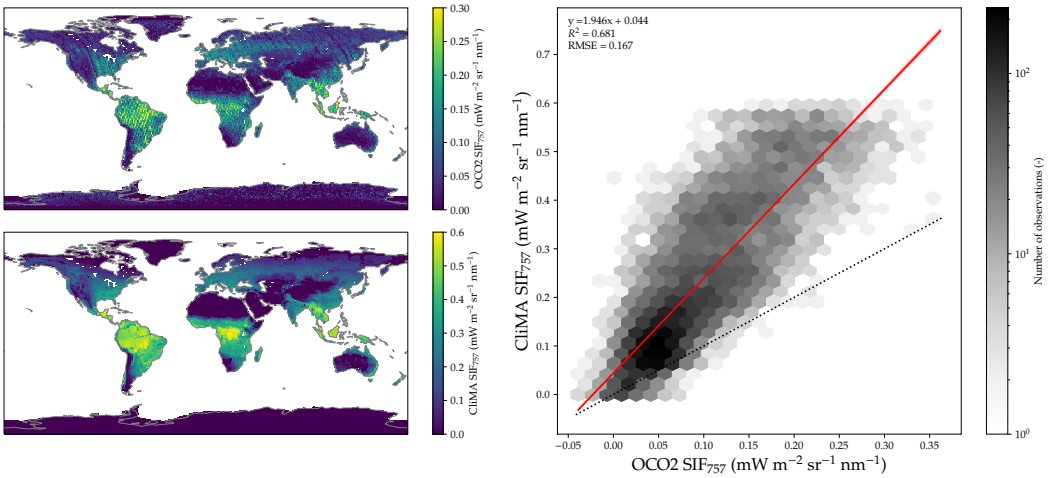

Figure 6. Comparison of solar induced chlorophyll fluorescence at 757 nm (SIF_{757}). CliMA Land global run was made for the year 2019. OCO-2 SIF_{757} was regridded from satellite retrievals. SIF_{757} was annual means averaged from monthly averages (nighttime values set to 0). Red solid line with shaded region plots the linear regression with confidence intervals, and black dotted line plots the 1:1 line.

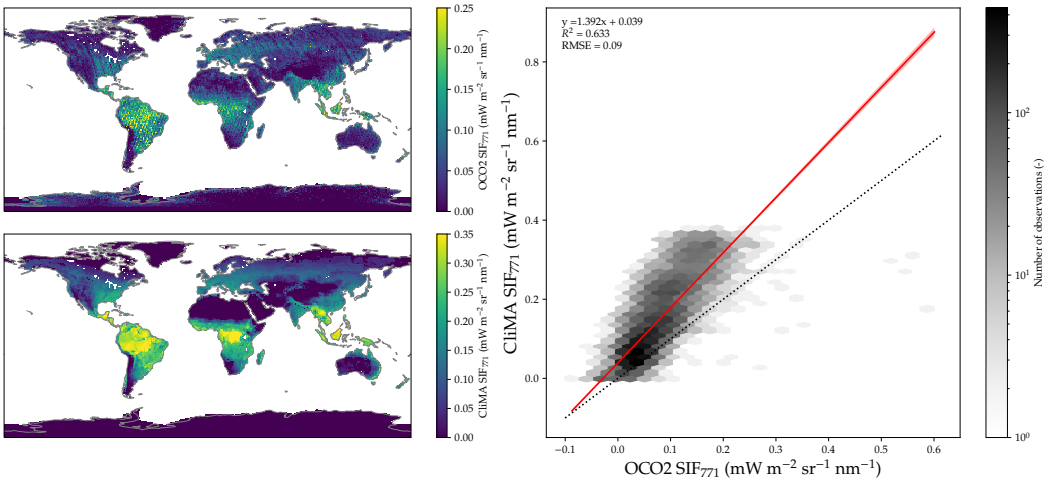

Figure 7. Comparison of solar induced chlorophyll fluorescence at 771 nm (SIF_{771}). CliMA Land global run was made for the year 2019. OCO-2 SIF_{771} was regridded from satellite retrievals. SIF_{771} was annual means averaged from monthly averages (nighttime values set to 0). Red solid line with shaded region plots the linear regression with confidence intervals, and black dotted line plots the 1:1 line.

3.4 NDVI

CliMA NDVI (average daytime values) well reproduced the pattern of MODIS NDVI (Figure 8). However, the two differed in their magnitude as CliMA NDVI was generally higher than MODIS NDVI by 0.1 ($y = 1.057x + 0.097$ and $R^2 = 0.915$; slope significantly different from 1; Figure 8).

3.5 EVI

Similar to the comparison with MODIS NDVI, CliMA EVI (average daytime values) also showed good agreement with MODIS EVI ($y = 1.372x + 0.067$ and $R^2 = 0.914$; slope significantly different from 1, $p < 0.001$; Figure 9).

3.6 NIRv

CliMA NIRv (average daytime values) well represented the spatial patterns observed from MODIS NIRv, but the two differed in their magnitudes ($y = 1.691x - 0.010$ and $R^2 = 0.875$; slope significantly different from 1, $p < 0.001$; Figure 10).

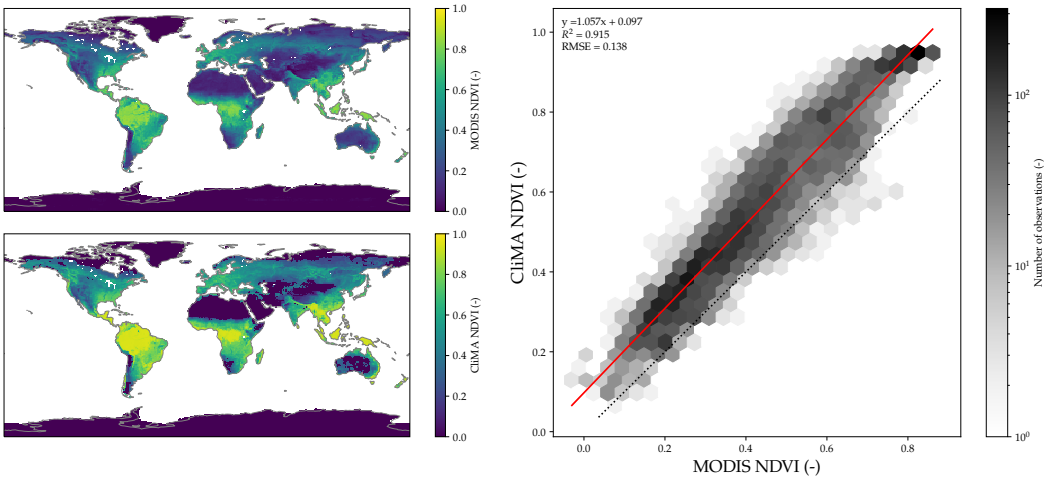

Figure 8. Comparison of normalized difference vegetation index (NDVI). CliMA Land global run was made for the year 2019. MODIS NDVI was regridded from satellite retrievals. NDVI was annual means averaged from 8-day averages (averaged from daytime values only). Red solid line with shaded region plots the linear regression with confidence intervals, and black dotted line plots the 1:1 line.

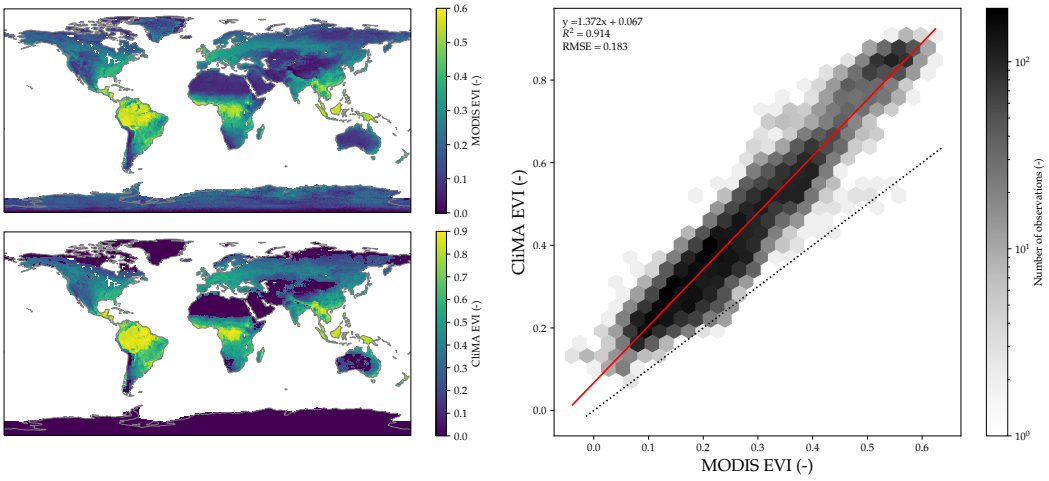

Figure 9. Comparison of enhanced vegetation index (EVI). CliMA Land global run was made for the year 2019. MODIS EVI was regridded from satellite retrievals. EVI was annual means averaged from 8-day averages (averaged from daytime values only). Red solid line with shaded region plots the linear regression with confidence intervals, and black dotted line plots the 1:1 line.

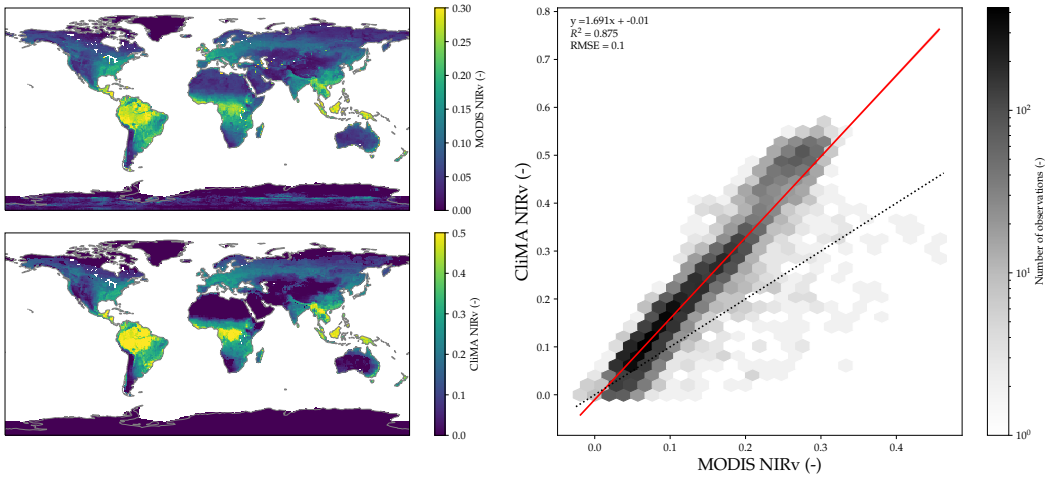

Figure 10. Comparison of near infrared reflectance of vegetation (NIRv). CliMA Land global run was made for the year 2019. MODIS NIRv was regridded from satellite retrievals. NIRv was annual means averaged from 8-day averages (averaged from daytime values only). Red solid line with shaded region plots the linear regression with confidence intervals, and black dotted line plots the 1:1 line.

3.7 ILAMB

The ILAMB results showed that CliMA Land had higher discrepancies with the reference estimate (MPI RS+METEO GPP) than the Ensemble CMIP5 (from 8 models) and the Ensemble CMIP6 (from 12 models). The discrepancies were larger both in terms of bias score and root-mean-square-error (RSME) in GPP, as CliMA Land predicted approximately 34% higher GPP than MPI RS+METEO GPP (CliMA Land GPP was 155.1 Pg C $year^{-1}$ and MPI RS+METRO GPP was 115.7 Pg C $year^{-1}$ for the year 2010). In terms of seasonal cycle score of GPP, CliMA Land performed similarly to Ensemble CMIP6, both of which showed better agreement with MPI RS+METEO GPP than the Ensemble CMIP5. Overall, CliMA Land was less closer to MPI RS+METEO GPP than Ensemble CMIP5 and CMIP6 in GPP given the higher CliMA GPP than MPI RS+METEO GPP. See Y. Wang, Braghiere, and Frankenberh (2021) for the complete set of ILAMB results (also available at `https://braghiere.github.io/ILAMB_CliMA_gpp_et/index.html`). We note that CliMA Land input parameters have not yet been calibrated to match field- or satellite-based measurements, and future calibrations will improve the model predictive

skills. It is also worth noting that MPI RS+METEO GPP is also an estimate of GPP and thus has significant uncertainty.

4 Discussion

We present and evaluate CliMA Land, the first LSM that can simultaneously simulate hyperspectral canopy fluorescence and reflectance properties as well as corresponded carbon and water fluxes. CliMA Land modeled indices and measures, in general, well captured the spatial patterns globally, though the magnitude differed in some regions. These inconsistencies between model outputs and data-driven estimates potentially resulted from the following aspects, improvements over which would advance future land modeling.

(i) CliMA Land is not well constrained given the various sources of plant traits and environmental cues. First, the model input datasets often disagree in their assumptions and model complexity, likely resulting in biases in simulated results (see Y. Wang and Frankenberg (2021) for an example of how canopy model complexity impacts the simulated carbon, water, and fluorescence fluxes). Second, because of the limited knowledge of how plant physiological traits vary spatially and temporally, datasets used to drive CliMA Land are often temporally constant instead of a time series. For instance, photosynthetic capacity represented by V_{cmax25}, which should be varying in a growing season, is constant in a grid in our simulation, and this might contribute biases in the simulated carbon and water fluxes (Y. P. Wang et al., 2007). Third, CliMA Land prescribed environmental cues from ERA5 reanalysis data, which were interpolated from sparsely distributed historical observations and could have high uncertainty; and mismatch between ERA5 reanalysis data and reality would also contribute to biases in our model output. For example, when comparing the soil water contents from ERA5 reanalysis (black curve in Figure S1) vs. that from flux tower measurements (red curve with shaded region in Figure S1), we found that ERA5 reanalysis data had wetter soil throughout the year, particularly from day 1 to 150, which corresponded to the growing season at AU-Tum. Promisingly, with the increasing number of observations across the globe, the uncertainty and biases resulting from model parameterization will be better resolved in the future (Cucchi et al., 2020).

(ii) Some key processes have been missing in the global-scale LSMs, such as the dynamics and variations in leaf photosynthesis and fluorescence related physiology. For example, Magney et al. (2019) and Raczka et al. (2019) highlighted the importance of sustained non-photochemical quenching (NPQ) in modeling SIF in the cold winter, which results in lower modeled SIF in cold environments. However, this process has not been yet implemented in any land surface or vegetation model (including CliMA Land) because of the lack of knowledge on how sustained NPQ quantitatively and mechanistically responds to temperature. Also, we used constant parameter sets for rate coefficient calculations such as the temperature dependency of maximum carboxylation rate, whereas species- and temperature-dependent parameter sets (Medlyn et al., 2002) should be used to best describe plants' acclimation to the environment. Similarly, the fluorescence parameter set we used to compute NPQ, fluorescence yield, and hence SIF (see van der Tol et al. (2014) for more details), was also constant across the globe, regardless of the site-level species composition and stress status. Future research efforts to implement new physiological processes and resolve the spatial and temporal variations and acclimation of these physiological parameters will also improve the predictive skills of LSMs.

(iii) The global scale data-driven GPP estimation used in the present study was interpolated using machine learning based on algorithm rather than real observations at $1^\circ \times 1^\circ$ resolution, and thus had high uncertainty in the grids without a flux tower. Further, even for those grids with flux towers, there could be issues when up scaling flux tower observations that typically covers < 1 km^2 footprint to the entire grid that may range up to > 10000 km^2 and consist various vegetation types. A recent study compared 45 global GPP products and found considerable difference among the products, and the annual GPP ranges from approximately 0.8 to 2.4 times the MPI GPP (Zhang & Ye, 2021). In comparison, CliMA GPP was 1.26 times the MPI GPP for the year 2019. Therefore, as true global GPP patterns are unknown and current estimates are highly inconsistent (Anav et al., 2015; Zhang & Ye, 2021), effective evaluation of CliMA GPP or any other GPP remains a challenge.

(iv) The global-scale TROPOMI, OCO-2, and MODIS observations may have considerable errors. For example, the retrievals are often negative or close to zero, particularly in those regions with low vegetation cover, making it difficult for a 1:1 comparison between CliMA Land output and satellite observations. As a result, there

is always a postive offset in the linear regressions. For example, SIF retrieval may use barren land as a baseline, and the potential illuminance from other chemicals other than chlorophyll could lead to biases over the baseline (Köhler et al., 2021). Moreover, the mismatch in sun-sensor geometry likely impacted the 1:1 comparison between CliMA Land and TROPOMI/OCO-2 SIF as we used a nadir viewing zenith angle for the global simulation. We note that the daily average SIF in CliMA Land was calculated by averaging the SIF at nadir throughout the diurnal cycle, whereas TROPOMI/OCO-2 daily mean SIF was converted from point measurements with varying solar zenith angles based on an assumption that SIF is a function of cosine solar zenith angle that peaks at midday, which may not be true. We not that CliMA Land allows for using specific sun-sensor geometry and solar time that match all satellite overpasses, enabling the direct comparison between model simulation and satellite retrievals rather than the averages (as done in Figure 16 of Y. Wang, Köhler, et al., 2021). As CliMA Land is equipped to utilize the data from multiple sources, such as flux tower and satellite observations, it allows for more systematic and comprehensive data assimilation, thus promoting future research on plant trait inversion at various spatial and temporal resolutions.

We note that CliMA predictions (pure forward model run without parameter calibration) were generally higher than existing MPI, TROPOMI, OCO-2, and MODIS products. Aside from errors in the reference benchmark datasets, the differences probably resulted from non-idealized model parameterization, such as chlorophyll content which was not inverted to use with a hyperspectral and multi-layer canopy RT model (so did many other input parameters). For example, if we use a lower chlorophyll content in the model, the vegetation will be less greener and thus NDVI, EVI, and NIRv will be lower; SIF and GPP will also be lower given the lower PAR absorption. Being able to simultaneously model hyperspectral canopy RT as well as carbon and water fluxes, CliMA Land has great potential in advancing future Earth System modeling. The simulated hyperspectral canopy RT can be directly compared to satellite observations, and can help constrain the Earth system model with the large number of remote sensing data such as inverting chlorophyll content that (1) is compatible with hyperspectral and multi-layer canopy RT model, and (2) agrees with remote sensing and/or ground-based data from multiple sources.

Further, the high temporal resolution of CliMA Land outputs provides an improved way to interpolate observations using modeled patterns (compared to prescribed constant trends such as when computing daily average SIF). The hourly global scales simulations allow for novel research that was not feasible in the past, such as the decoupling of SIF and NIRv vs. GPP in a diurnal cycle under different environmental stresses, supplementing the deficits of traditional satellite retrievals. We believe that future global maps with improved temporal resolutions (e.g., the NASA Surface Biology and Geology mission) can be used as model inputs, and that the implementation of new features into the land model will advance the land model predictive skills, for not only the past but also the future climate with respect to global climate change.

5 Conclusions

We present our first global run of CliMA Land, the first global land surface model that outputs carbon and water fluxes as well as hyperspectral canopy reflectance and fluorescence simultaneously. CliMA Land allows for not only the comparison of spatial patterns between carbon and water fluxes, reflectance, and chlorophyll fluorescence, but also provides insight into the details of their diurnal and seasonal cycles. We compare the model outputs to other data-driven GPP, SIF, NDVI, EVI, and NIRv products, and demonstrate the predictive skills of CliMA Land. Our model simulations underline (i) the necessity of improving land model parameterization, both spatially and temporally; (ii) the importance of implementing advanced or new features in the land surface models, such as the photosynthesis and fluorescence physiology; and (iii) the demand of integrating datasets to calibrate land surface models.

Acknowledgements

We gratefully acknowledge the generous support of Eric and Wendy Schmidt (by recommendation of the Schmidt Futures) and the Heising-Simons Foundation. This research has been supported by the National Aeronautics and Space Administration (NASA) Earth Sciences Division grant NNX15AH95G and NASA Carbon Cycle Science grant 80NSSC21K1712 awarded to Christian Frankenberg. M.L. was supported by the NASA Postdoctoral Program, administered by Universities Space Research Association under contract with NASA, and by the Next Generation Ecosystem

Experiments-Tropics, funded by the U.S. Department of Energy, Office of Science, Office of Biological and Environmental Research. Part of this research was carried out at the Jet Propulsion Laboratory, California Institute of Technology, under a contract with NASA. California Institute of Technology. Government sponsorship acknowledged. ERA5 data were generated using Copernicus Climate Change Service Information. Neither the European Commission nor the European Centre for Medium-Range Weather Forecasts (ECMWF) are responsible for any use that may be made of the Copernicus information or data in this publication. We gratefully thank Dr. Butler, Croft, Dai, He, Lawrence, Luo, Simard, Yamazaka, and Yuan for sharing the gridded datasets.

References

Anav, A., Friedlingstein, P., Beer, C., Ciais, P., Harper, A., Jones, C., ... Zhao, M. (2015). Spatiotemporal patterns of terrestrial gross primary production: A review. *Reviews of Geophysics*, *53*(3), 785–818.

Anav, A., Friedlingstein, P., Kidston, M., Bopp, L., Ciais, P., Cox, P., ... Zhu, Z. (2013). Evaluating the land and ocean components of the global carbon cycle in the CMIP5 earth system models. *Journal of Climate*, *26*(18), 6801–6843.

Anderegg, W. R., Wolf, A., Arango-Velez, A., Choat, B., Chmura, D. J., Jansen, S., ... Pacala, S. (2018). Woody plants optimise stomatal behaviour relative to hydraulic risk. *Ecology Letters*, *21*(7), 968–977.

Anderegg, W. R. L., Schwalm, C., Biondi, F., Camarero, J. J., Koch, G., Litvak, M., ... Pacala, S. (2015). Pervasive drought legacies in forest ecosystems and their implications for carbon cycle models. *Science*, *349*(6247), 528–532.

Arora, V. K., Boer, G. J., Friedlingstein, P., Eby, M., Jones, C. D., Christian, J. R., ... Wu, T. (2013). Carbon–concentration and carbon–climate feedbacks in CMIP5 earth system models. *Journal of Climate*, *26*(15), 5289–5314.

Badgley, G., Anderegg, L. D., Berry, J. A., & Field, C. B. (2019). Terrestrial gross primary production: Using nirv to scale from site to globe. *Global change biology*, *25*(11), 3731–3740.

Badgley, G., Field, C. B., & Berry, J. A. (2017). Canopy near-infrared reflectance and terrestrial photosynthesis. *Science advances*, *3*(3), e1602244.

Baldocchi, D. D. (2020). How eddy covariance flux measurements have contributed to our understanding of global change biology. *Global change biology*, *26*(1), 242–260.

Baldocchi, D. D., Falge, E., Gu, L., Olson, R., Hollinger, D., Running, S., ... Wofsy, S. (2001). FLUXNET: A new tool to study the temporal and spatial variability of ecosystem-scale carbon dioxide, water vapor, and energy flux densities. *Bulletin of the American Meteorological Society*, *82*(11), 2415–2434.

Ball, J. T., Woodrow, I. E., & Berry, J. A. (1987). A model predicting stomatal conductance and its contribution to the control of photosynthesis under different environmental conditions. In *Progress in photosynthesis research* (pp. 221–224). Springer.

Bonan, G. B., Patton, E. G., Finnigan, J. J., Baldocchi, D. D., & Harman, I. N. (2021). Moving beyond the incorrect but useful paradigm: reevaluating big-leaf and multilayer plant canopies to model biosphere-atmosphere fluxes–a review.

Agricultural and Forest Meteorology, *306*, 108435.

Bonan, G. B., Patton, E. G., Harman, I. N., Oleson, K. W., Finnigan, J. J., Lu, Y., & Burakowski, E. A. (2018). Modeling canopy-induced turbulence in the earth system: A unified parameterization of turbulent exchange within plant canopies and the roughness sublayer (clm-ml v0). *Geoscientific Model Development*, *11*(4), 1467–1496.

Braghiere, R. K., Quaife, T., Black, E., He, L., & Chen, J. (2019). Underestimation of global photosynthesis in earth system models due to representation of vegetation structure. *Global Biogeochemical Cycles*, *33*(11), 1358–1369.

Braghiere, R. K., Quaife, T., Black, E., Ryu, Y., Chen, Q., De Kauwe, M. G., & Baldocchi, D. (2020). Influence of sun zenith angle on canopy clumping and the resulting impacts on photosynthesis. *Agricultural and Forest Meteorology*, *291*, 108065.

Braghiere, R. K., Wang, Y., Doughty, R., Sousa, D., Magney, T., Widlowski, J.-L., ... Frankenberg, C. (2021). Accounting for canopy structure improves hyperspectral radiative transfer and sun-induced chlorophyll fluorescence representations in a new generation earth system model. *Remote Sensing of Environment*, *261*, 112497.

Butler, E. E., Datta, A., Flores-Moreno, H., Chen, M., Wythers, K. R., Fazayeli, F., ... Reich, P. B. (2017). Mapping local and global variability in plant trait distributions. *Proceedings of the National Academy of Sciences*, *114*(51), E10937–E10946.

Campbell, G. S., & Norman, J. M. (1998). *An introduction to environmental biophysics*. Springer Science & Business Media, New York, New York, USA.

Collier, N., Hoffman, F. M., Lawrence, D. M., Keppel-Aleks, G., Koven, C. D., Riley, W. J., ... Randerson, J. T. (2018). The international land model benchmarking (ilamb) system: design, theory, and implementation. *Journal of Advances in Modeling Earth Systems*, *10*(11), 2731–2754.

Croft, H., Chen, J., Wang, R., Mo, G., Luo, S., Luo, X., ... Bonal, D. (2020). The global distribution of leaf chlorophyll content. *Remote Sensing of Environment*, *236*, 111479.

Cucchi, M., Weedon, G. P., Amici, A., Bellouin, N., Lange, S., Müller Schmied, H., ... Buontempo, C. (2020). Wfde5: bias-adjusted era5 reanalysis data for impact studies. *Earth System Science Data*, *12*(3), 2097–2120.

Dai, Y., Xin, Q., Wei, N., Zhang, Y., Shangguan, W., Yuan, H., ... Lu, X. (2019). A global high-resolution data set of soil hydraulic and thermal properties for land surface modeling. *Journal of Advances in Modeling Earth Systems*, *11*(9), 2996–3023.

De Kauwe, M. G., Kala, J., Lin, Y.-S., Pitman, A. J., Medlyn, B. E., Duursma, R. A., ...

Miralles, D. G. (2015). A test of an optimal stomatal conductance scheme within the cable land surface model. *Geoscientific Model Development*, *8*(2), 431–452.

Doughty, R., Xiao, X., Köhler, P., Frankenberg, C., Qin, Y., Wu, X., ... Moore III, B. (2021). Global-scale consistency of spaceborne vegetation indices, chlorophyll fluorescence, and photosynthesis. *Journal of Geophysical Research: Biogeosciences*, e2020JG006136.

Eller, C. B., Rowland, L., Oliveira, R. S., Bittencourt, P. R. L., Barros, F. V., da Costa, A. C. L., ... Cox, P. (2018). Modelling tropical forest responses to drought and El Niño with a stomatal optimization model based on xylem hydraulics. *Philosophical Transactions of the Royal Society B: Biological Sciences*, *373*(1760), 20170315.

Frankenberg, C., Fisher, J. B., Worden, J., Badgley, G., Saatchi, S. S., Lee, J.-E., ... Yokota, T. (2011). New global observations of the terrestrial carbon cycle from gosat: Patterns of plant fluorescence with gross primary productivity. *Geophysical Research Letters*, *38*(17).

He, L., Chen, J. M., Pisek, J., Schaaf, C. B., & Strahler, A. H. (2012). Global clumping index map derived from the modis brdf product. *Remote Sensing of Environment*, *119*, 118–130.

Helm, L. T., Shi, H., Lerdau, M. T., & Yang, X. (2020). Solar-induced chlorophyll fluorescence and short-term photosynthetic response to drought. *Ecological Applications*, *30*(5), e02101.

Hersbach, H., Bell, B., Berrisford, P., Biavati, G., Horányi, A., Muñoz Sabater, J., ... Thépaut, J.-N. (2018). Era5 hourly data on single levels from 1979 to present. *Copernicus Climate Change Service (C3S) Climate Data Store (CDS)*, (Accessed on 04-Aug-2021), 10.24381/cds.adbb2d47.

Hersbach, H., Bell, B., Berrisford, P., Hirahara, S., Horányi, A., Muñoz-Sabater, J., ... Thépaut, J.-N. (2020). The ERA5 global reanalysis. *Quarterly Journal of the Royal Meteorological Society*, *146*(730), 1999–2049.

Jiang, C., & Fang, H. (2019). Gsv: a general model for hyperspectral soil reflectance simulation. *International Journal of Applied Earth Observation and Geoinformation*, *83*, 101932.

Jones, C., Robertson, E., Arora, V., Friedlingstein, P., Shevliakova, E., Bopp, L., ... Tjiputra, J. (2013). Twenty-first-century compatible CO_2 emissions and airborne fraction simulated by CMIP5 earth system models under four representative concentration pathways. *Journal of Climate*, *26*(13), 4398–4413.

Jung, M., Reichstein, M., Margolis, H. A., Cescatti, A., Richardson, A. D., Arain, M. A., ... Williams, C. (2011). Global patterns of land-atmosphere fluxes of carbon dioxide, latent heat, and sensible heat derived from eddy covariance, satellite, and meteorological observations. *Journal of Geophysical Research: Biogeosciences*, *116*(G3).

Jung, M., Reichstein, M., Schwalm, C. R., Huntingford, C., Sitch, S., Ahlström, A., ... Zeng, N. (2017). Compensatory water effects link yearly global land CO_2 sink changes to temperature. *Nature*, *541*(7638), 516–520.

Jung, M., Schwalm, C., Migliavacca, M., Walther, S., Camps-Valls, G., Koirala, S., ... Reichstein, M. (2020). Scaling carbon fluxes from eddy covariance sites to globe: synthesis and evaluation of the fluxcom approach. *Biogeosciences*, *17*(5), 1343–1365.

Kennedy, D., Swenson, S., Oleson, K. W., Lawrence, D. M., Fisher, R., Lola da Costa, A. C., & Gentine, P. (2019). Implementing plant hydraulics in the community land model, version 5. *Journal of Advances in Modeling Earth Systems*, *11*(2), 485–513.

Köhler, P., Fischer, W. W., Rossman, G. R., Grotzinger, J. P., Doughty, R., Wang, Y., ... Frankenberg, C. (2021). Mineral luminescence observed from space. *Geophysical Research Letters*, *48*(19), e2021GL095227.

Köhler, P., Frankenberg, C., Magney, T. S., Guanter, L., Joiner, J., & Landgraf, J. (2018). Global retrievals of solar-induced chlorophyll fluorescence with TROPOMI: First results and intersensor comparison to OCO-2. *Geophysical Research Letters*, *45*(19), 10,456–10,463.

Konings, A. G., Saatchi, S. S., Frankenberg, C., Keller, M., Leshyk, V., Anderegg, W. R., ... Zuidema, P. A. (2021). Detecting forest response to droughts with global observations of vegetation water content. *Global change biology*, *27*(23), 6005–6024.

Lawrence, D. M., Fisher, R. A., Koven, C. D., Oleson, K. W., Swenson, S. C., Bonan, G., ... Zeng, X. (2019). The community land model version 5: Description of new features, benchmarking, and impact of forcing uncertainty. *Journal of Advances in Modeling Earth Systems*, *11*(12), 4245–4287.

Lawrence, P. J., & Chase, T. N. (2007). Representing a new modis consistent land surface in the community land model (clm 3.0). *Journal of Geophysical Research: Biogeosciences*, *112*, G01023.

Le Quéré, C., Andrew, R. M., Friedlingstein, P., Sitch, S., Pongratz, J., Manning, A. C., ... Zhu, D. (2018). Global carbon budget 2017. *Earth System Science Data*, *10*(1), 405–448.

Leuning, R. (1995). A critical appraisal of a combined stomatal-photosynthesis model for C_3 plants. *Plant, Cell & Environment*, *18*(4), 339–355.

Luo, X., Keenan, T. F., Chen, J. M., Croft, H., Colin Prentice, I., Smith, N. G., ... Zhang, Y. (2021). Global variation in the fraction of leaf nitrogen allocated to photosynthesis. *Nature Communications*, *12*(1), 4866.

Magney, T. S., Barnes, M. L., & Yang, X. (2020). On the covariation of chlorophyll fluorescence and photosynthesis across scales. *Geophysical Research Letters*, *47*(23), e2020GL091098.

Magney, T. S., Bowling, D. R., Logan, B. A., Grossmann, K., Stutz, J., Blanken, P. D., ... Frankenberg, C. (2019). Mechanistic evidence for tracking the seasonality of photosynthesis with solar-induced fluorescence. *Proceedings of the National Academy of Sciences*, *116*(24), 11640–11645.

Marengo, J. A., Cunha, A. P., Cuartas, L. A., Deusdará Leal, K. R., Broedel, E., Seluchi, M. E., ... Bender, F. (2021). Extreme drought in the brazilian pantanal in 2019–2020: Characterization, causes, and impacts. *Frontiers in Water*, *3*, 13.

Marrs, J., Reblin, J., Logan, B., Allen, D., Reinmann, A., Bombard, D., ... Hutyra, L. (2020). Solar-induced fluorescence does not track photosynthetic carbon assimilation following induced stomatal closure. *Geophysical Research Letters*, *47*(15), e2020GL087956.

Medlyn, B. E., Dreyer, E., Ellsworth, D., Forstreuter, M., Harley, P. C., Kirschbaum, M. U. F., ... Loustau, D. (2002). Temperature response of parameters of a biochemically based model of photosynthesis. II. A review of experimental data. *Plant, Cell & Environment*, *25*(9), 1167–1179.

Medlyn, B. E., Duursma, R. A., Eamus, D., Ellsworth, D. S., Prentice, I. C., Barton, C. V. M., ... Wingate, L. (2011). Reconciling the optimal and empirical approaches to modelling stomatal conductance. *Global Change Biology*, *17*(6), 2134–2144.

Medlyn, B. E., Duursma, R. A., & Zeppel, M. J. (2011). Forest productivity under climate change: a checklist for evaluating model studies. *Wiley Interdisciplinary Reviews: Climate Change*, *2*(3), 332–355.

Norby, R. J., Gu, L., Haworth, I. C., Jensen, A. M., Turner, B. L., Walker, A. P., ... Winter, K. (2017). Informing models through empirical relationships between foliar phosphorus, nitrogen and photosynthesis across diverse woody species in tropical forests of panama. *New Phytologist*, *215*(4), 1425–1437.

Norton, A. J., Rayner, P. J., Koffi, E. N., & Scholze, M. (2018). Assimilating solar-induced chlorophyll fluorescence into the terrestrial biosphere model bethy-scope v1.0: model description and information content. *Geoscientific Model Development*, *11*(4), 1517–1536.

Norton, A. J., Rayner, P. J., Koffi, E. N., Scholze, M., Silver, J. D., & Wang, Y.-P. (2019). Estimating global gross primary productivity using chlorophyll fluorescence and a data assimilation system with the bethy-scope model. *Biogeosciences*, *16*(15), 3069–3093.

Pastorello, G., Trotta, C., Canfora, E., Chu, H., Christianson, D., Cheah, Y.-W., ... Papale, D. (2020). The FLUXNET2015 dataset and the ONEFlux processing pipeline for eddy covariance data. *Scientific Data*, *7*(1), 225.

Pinty, B., Lavergne, T., Dickinson, R., Widlowski, J.-L., Gobron, N., & Verstraete, M. (2006). Simplifying the interaction of land surfaces with radiation for relating remote sensing products to climate models. *Journal of Geophysical Research: Atmospheres*, *111*(D2).

Powell, T. L., Galbraith, D. R., Christoffersen, B. O., Harper, A., Imbuzeiro, H., Rowland, L., ... Moorcroft, P. R. (2013). Confronting model predictions of carbon fluxes with measurements of Amazon forests subjected to experimental drought. *New Phytologist*, *200*(2), 350–365.

Qiu, B., Chen, J. M., Ju, W., Zhang, Q., & Zhang, Y. (2019). Simulating emission and scattering of solar-induced chlorophyll fluorescence at far-red band in global vegetation with different canopy structures. *Remote Sensing of Environment*, *233*, 111373.

Raczka, B., Porcar-Castell, A., Magney, T., Lee, J. E., Köhler, P., Frankenberg, C., ... Bowling, D. R. (2019). Sustained nonphotochemical quenching shapes the seasonal pattern of solar-induced fluorescence at a high-elevation evergreen forest. *Journal of Geophysical Research: Biogeosciences*, *124*(7), 2005–2020.

Reid, R. C., Prausnitz, J. M., & Poling, B. E. (1987). *The properties of gases and liquids*. McGraw Hill Book Co., New York, NY.

Schaaf, C., & Wang, Z. (2015). *Mcd43a4 modis/terra+aqua brdf/albedo nadir brdf adjusted ref daily l3 global - 500m v006.* NASA EOSDIS Land Processes DAAC. Retrieved from `https://lpdaac.usgs.gov/products/mcd43a4v006` doi: 10.5067/MODIS/MCD43A4.006

Schimel, D., Pavlick, R., Fisher, J. B., Asner, G. P., Saatchi, S., Townsend, P., ... Cox, P. (2015). Observing terrestrial ecosystems and the carbon cycle from space. *Global Change Biology*, *21*(5), 1762–1776.

Schimel, D., Schneider, F. D., Carbon, J., & Participants, E. (2019). Flux towers in the sky: global ecology from space. *New Phytologist*, *224*(2), 570–584.

Shiklomanov, A. N., Dietze, M. C., Fer, I., Viskari, T., & Serbin, S. P. (2021). Cutting out the middleman: calibrating and validating a dynamic vegetation model (ed2-prospect5) using remotely sensed surface reflectance. *Geoscientific Model Development*, *14*(5), 2603–2633.

Simard, M., Pinto, N., Fisher, J. B., & Baccini, A. (2011). Mapping forest canopy height globally with spaceborne lidar. *Journal of Geophysical Research: Biogeosciences*, *116*(G4021).

Sperry, J. S., & Love, D. M. (2015). What plant hydraulics can tell us about responses to climate-change droughts. *New Phytologist*, *207*(1), 14–27.

Sperry, J. S., Venturas, M. D., Anderegg, W. R. L., Mencuccini, M., Mackay, D. S., Wang, Y., & Love, D. M. (2017). Predicting stomatal responses to the environment from the optimization of photosynthetic gain and hydraulic cost. *Plant, Cell & Environment*, *40*(6), 816–830.

Sperry, J. S., Venturas, M. D., Todd, H. N., Trugman, A. T., Anderegg, W. R. L., Wang, Y., & Tai, X. (2019). The impact of rising CO_2 and acclimation on the response of US forests to global warming. *Proceedings of the National Academy of Sciences*, *116*(51), 25734–25744.

Sperry, J. S., Wang, Y., Wolfe, B. T., Mackay, D. S., Anderegg, W. R. L., McDowell, N. G., & Pockman, W. T. (2016). Pragmatic hydraulic theory predicts stomatal responses to climatic water deficits. *New Phytologist*, *212*(3), 577–589.

Sun, Y., Frankenberg, C., Jung, M., Joiner, J., Guanter, L., Köhler, P., & Magney, T. (2018). Overview of Solar-Induced chlorophyll Fluorescence (SIF) from the Orbiting Carbon Observatory-2: Retrieval, cross-mission comparison, and global monitoring for GPP. *Remote Sensing of Environment*, *209*, 808–823.

Sun, Y., Frankenberg, C., Wood, J. D., Schimel, D., Jung, M., Guanter, L., ... others (2017). Oco-2 advances photosynthesis observation from space via solar-induced chlorophyll fluorescence. *Science*, *358*(6360).

Tramontana, G., Jung, M., Schwalm, C. R., Ichii, K., Camps-Valls, G., Ráduly, B., ...

Papale, D. (2016). Predicting carbon dioxide and energy fluxes across global fluxnet sites with regression algorithms. *Biogeosciences*, *13*(14), 4291–4313.

Trugman, A. T., Medvigy, D., Mankin, J. S., & Anderegg, W. R. L. (2018). Soil moisture stress as a major driver of carbon cycle uncertainty. *Geophysical Research Letters*, *45*(13), 6495–6503.

van der Tol, C., Berry, J., Campbell, P., & Rascher, U. (2014). Models of fluorescence and photosynthesis for interpreting measurements of solar-induced chlorophyll fluorescence. *Journal of Geophysical Research: Biogeosciences*, *119*(12), 2312–2327.

van der Tol, C., Verhoef, W., Timmermans, J., Verhoef, A., & Su, Z. (2009). An integrated model of soil-canopy spectral radiances, photosynthesis, fluorescence, temperature and energy balance. *Biogeosciences*, *6*(12).

van Genuchten, M. T. (1980). A closed-form equation for predicting the hydraulic conductivity of unsaturated soils. *Soil science society of America journal*, *44*(5), 892–898.

Venturas, M. D., Sperry, J. S., Love, D. M., Frehner, E. H., Allred, M. G., Wang, Y., & Anderegg, W. R. L. (2018). A stomatal control model based on optimization of carbon gain versus hydraulic risk predicts aspen sapling responses to drought. *New Phytologist*, *220*(3), 836–850.

Walker, A. P., Beckerman, A. P., Gu, L., Kattge, J., Cernusak, L. A., Domingues, T. F., ... Woodward, F. I. (2014). The relationship of leaf photosynthetic traits–V_{cmax} and J_{max}–to leaf nitrogen, leaf phosphorus, and specific leaf area: A meta-analysis and modeling study. *Ecology and Evolution*, *4*(16), 3218–3235.

Wang, Y., Anderegg, W. R., Venturas, M. D., Trugman, A. T., Yu, K., & Frankenberg, C. (2021). Optimization theory explains nighttime stomatal responses. *New Phytologist*, *230*(4), 1550–1561.

Wang, Y., Braghiere, R. K., & Frankenberh, C. (2021). *Global scale carbon and water fluxes and canopy spectra simulation using the clima land (v0.1).* CaltechDATA. Retrieved from `https://data.caltech.edu/records/2191` doi: 10.22002/D1.2191

Wang, Y., & Frankenberg, C. (2021). On the impact of canopy model complexity on simulated carbon, water, and solar-induced chlorophyll fluorescence fluxes. *Biogeosciences Discussions*, *2021*, 1–23. doi: 10.5194/bg-2021-214

Wang, Y., Köhler, P., He, L., Doughty, R., Braghiere, R. K., Wood, J. D., & Frankenberg, C. (2021). Testing stomatal models at the stand level in deciduous angiosperm and

evergreen gymnosperm forests using clima land (v0.1). *Geoscientific Model Development*, *14*(11), 6741–6763.

Wang, Y., Sperry, J. S., Anderegg, W. R. L., Venturas, M. D., & Trugman, A. T. (2020). A theoretical and empirical assessment of stomatal optimization modeling. *New Phytologist*, *227*, 311–325.

Wang, Y., Sperry, J. S., Venturas, M. D., Trugman, A. T., Love, D. M., & Anderegg, W. R. L. (2019). The stomatal response to rising CO_2 concentration and drought is predicted by a hydraulic trait-based optimization model. *Tree Physiology*, *39*, 1416–1427.

Wang, Y. P., Baldocchi, D., Leuning, R., Falge, E., & Vesala, T. (2007). Estimating parameters in a land-surface model by applying nonlinear inversion to eddy covariance flux measurements from eight fluxnet sites. *Global Change Biology*, *13*(3), 652–670.

Wehr, R., Munger, J., McManus, J., Nelson, D., Zahniser, M., Davidson, E., ... Saleska, S. (2016). Seasonality of temperate forest photosynthesis and daytime respiration. *Nature*, *534*(7609), 680–683.

Yamazaki, D., Ikeshima, D., Tawatari, R., Yamaguchi, T., O'Loughlin, F., Neal, J. C., ... Bates, P. D. (2017). A high-accuracy map of global terrain elevations. *Geophysical Research Letters*, *44*(11), 5844–5853.

Yang, P., Prikaziuk, E., Verhoef, W., & van der Tol, C. (2021). Scope 2.0: a model to simulate vegetated land surface fluxes and satellite signals. *Geoscientific Model Development*, *14*(7), 4697–4712.

Yang, P., Verhoef, W., & van der Tol, C. (2017). The mscope model: A simple adaptation to the scope model to describe reflectance, fluorescence and photosynthesis of vertically heterogeneous canopies. *Remote sensing of environment*, *201*, 1–11.

Yuan, H., Dai, Y., & Li, S. (2020). *Reprocessed MODIS version 6 leaf area index data sets for land surface and climate modelling.* Sun Yat-sun University. Retrieved from `http://globalchange.bnu.edu.cn/research/laiv6`

Yuan, H., Dai, Y., Xiao, Z., Ji, D., & Shangguan, W. (2011). Reprocessing the modis leaf area index products for land surface and climate modelling. *Remote Sensing of Environment*, *115*(5), 1171–1187.

Zhang, Y., Guanter, L., Berry, J. A., van der Tol, C., Yang, X., Tang, J., & Zhang, F. (2016). Model-based analysis of the relationship between sun-induced chlorophyll fluorescence and gross primary production for remote sensing applications. *Remote*

Sensing of Environment, *187*, 145–155.

Zhang, Y., Xiao, X., Wu, X., Zhou, S., Zhang, G., Qin, Y., & Dong, J. (2017). A global moderate resolution dataset of gross primary production of vegetation for 2000–2016. *Scientific data*, *4*, 170165.

Zhang, Y., & Ye, A. (2021). Would the obtainable gross primary productivity (gpp) products stand up? a critical assessment of 45 global gpp products. *Science of The Total Environment*, *783*, 146965.